

Wind line variability and intrinsic errors in observational mass loss rates

DERCK MASSA,¹ RAMAN K. PRINJA,² AND LIDIA OSKINOVA³

¹*Space Science Institute
4750 Walnut Street, Suite 205
Boulder, Colorado 80301, USA*

²*Department of Physics & Astronomy
University College London
Gower Street, London WC1E 6BT, UK*

³*Institute for Physics and Astronomy
University of Potsdam
Karl-Liebknecht-Str. 24/25, D-14476 Potsdam, Germany*

ABSTRACT

UV wind line variability in OB stars appears to be universal. In order to quantify this variation and to estimate its effect on a mass loss rate determined from a single observation, we use the *IUE* archive to identify non-peculiar OB stars with well developed but unsaturated Si IV $\lambda 1400$ doublets and at least 10 independent observations. This resulted in 1699 spectra of 25 stars. A simple model was used to translate the observed profile variations into optical depth variations and, hence, variations in measured mass loss rates. These variations quantify the *intrinsic error* inherent in any single mass loss rate derived from a single observation. The derived rates have an overall 1σ variation of about 22%, but this appears to differ with T_{eff} , being as small as 8% for the hottest stars and up to 45% for the cooler ones. Furthermore, any single determination can differ from the mean by a factor of 2 or more. Our results also imply that mass loss rates determined from non-simultaneous observations (such as UV and ground based data) need not agree. In addition, we use our results to examine the nature of the structures responsible for the variability. Our findings suggest that the optical depth variations result from optically very thick structures occulting more or less of the line of sight to the stellar disk. Further, the smaller optical depth variations in the hottest stars suggests that the structures responsible for the variations are disrupted in their more powerful winds.

Keywords: Early-type stars(430) — Ultraviolet spectroscopy(2284) — Stellar winds(1636) — Stellar mass loss(1613)

1. INTRODUCTION

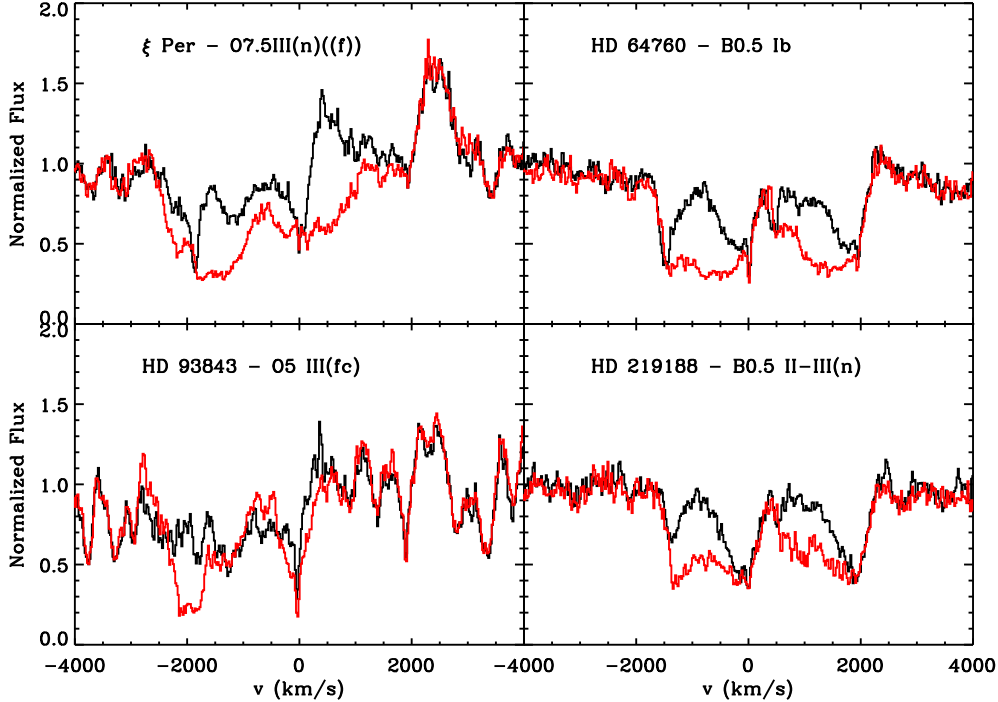


Figure 1. Examples of Si IV $\lambda\lambda 1400$ variability in four stars with a range in spectral types, demonstrating the ubiquity of wind line variation.

It is well known that the winds of massive stars help to power the interstellar medium and contribute to determining how OB stars will end their nuclear burning lifetime and the nature of their remnants. Consequently, it is important to understand the mechanisms responsible for mass loss and our ability to measure it. One complication to achieving this is that the winds of massive stars are variable.

Wind line variability, as seen in H α , has been known for many years (e.g. Ebbets 1982). With the advent of the *International Ultraviolet Explorer*, *IUE*, it became clear that virtually all well developed but unsaturated UV wind lines in OB stars were highly variable (e.g. Prinja & Howarth 1986; Massa et al. 1995; Kaper et al. 1996; Prinja et al. 2002, Figure 1). Later studies demonstrated that the wind lines of LMC and SMC OB stars vary as well (Massa et al. 2000; Lehner et al. 2003), and that the wind lines of the central stars of planetary nebulae show similar variations (Prinja et al. 2012). Consequently, it is important to understand the nature of the variability because *wind line variability appears to be a universal property of radiatively driven winds*.

In addition to universality, studies have revealed much about the nature of wind line variability and its origin. First, it is repetitive, on a time scale on the order of the stellar rotation period (Prinja 1988). Second, once a feature is detected at low velocity, it persists to the terminal velocity (Kaper et al. 1996; Massa et al. 1995; de Jong et al. 2001; Prinja et al. 2002), suggesting that the structures

are very large and probably due to spiral features in the wind (Prinja & Howarth 1988). Third, the structures originate at or very near the stellar surface (Howarth et al. 1995; Massa & Prinja 2015). Fourth, for B supergiants it has been shown that the structures are optically very thick and cover a large portion of the face of the star (e.g. Prinja & Massa 2010). Fifth, X-ray observations imply that the structures are considerably denser than the rest of the wind (Massa et al. 2019). Sixth, when a star is viewed nearly equator on, the wavelength dependence of the variability presents a pattern indicative of large spiral structures in the wind (Cranmer & Owocki 1996; Fullerton et al. 1997; de Jong et al. 2001).

All of these factors affect the wind diagnostics and how we convert them into mass loss rates. One consequence of this is that the four different means to measure mass loss rates (\dot{M}): wind lines, IR/Radio excesses, X-ray emissions and bow shocks, do not all agree (e.g. Fullerton et al. 2006; Massa et al. 2017; Kobulnicky et al. 2019). The most likely reason is that current models do not adequately represent the density structures (clumping) in the winds.

Observations of wind line variability present an opportunity to characterize the wind structures responsible for the variability and to determine the intrinsic accuracy of a single measurement of \dot{M} . In this paper, we address the effects of wind line variability quantitatively. We consider its effect on mass loss rate diagnostics and what it might reveal about the physical nature and geometry of the structures responsible for the variability. This is done by fitting repeated *IUE* observations of the same star using the Sobolev approximation with exact integration model, (SEI, Lamers et al. 1987) and then examining the variations in the optical depths of the wind lines, which are proportional to $\dot{M}q$, where q is the ionization fraction of the ion being analyzed. We also allow the ratio of f values for the doublet to be variable, as this has been shown to be a coarse measure of the amount of optically thick clumping in the wind (Prinja & Massa 2010).

In the following, we explain why we concentrate on the Si IV doublet and present the sample of stars analyzed. Next, we detail how the wind lines are fit. We then analyze our results and discuss their implications. A final section summarizes our findings.

2. THE SAMPLE

To produce our sample, we began with all O and B III-I stars observed by *IUE* at high resolution with the short wavelength prime (SWP) camera, which covered the wavelength range $1150 \lesssim \lambda \lesssim 2000 \text{ \AA}$ with a resolution of $\simeq 15 \text{ km s}^{-1}$. We did this using the *IUE* archive at the Mikulski Archive for Space Telescopes (MAST). This sample was then restricted to stars that had 10 or more well exposed spectra. Stars were observed repeatedly by *IUE* for a multitude of reasons. It was common practice to obtain multiple exposures to increase the relatively low signal-to-noise of a single *IUE* spectrum. Some stars were monitored for calibration purposes, and others to search for variability.

We then eliminated all peculiar stars such as, Be stars, extremely rapid rotators, interacting binaries and X-ray binaries. Finally, we limited the sample to stars with well developed but unsaturated Si IV $\lambda 1400$ doublets. We concentrate on this doublet because it has the largest doublet separation of the wind lines available to *IUE*. Letting λ_B and λ_R denote the blue and red wavelengths of a doublet, the velocity separation of the doublet is given by the parameter $\delta \equiv c(\lambda_R - \lambda_B)/\lambda_B \text{ km s}^{-1}$. For Si IV, λ_B and λ_R are 1393.755 and 1402.750 \AA , so $\delta = 1936 \text{ km s}^{-1}$. In contrast, it is only 499 km s^{-1} for the C IV $\lambda 1550$ doublet. As a result of the large doublet separation, the components of the Si IV lines are less entangled (see the discussion of common point surfaces by Olson 1982), and that will be important for the fitting described in § 3. The restriction of the sample to stars with well

developed but unsaturated Si IV wind lines results in a sample consisting primarily of O and early B stars above the main sequence (see Walborn et al. 1985, 1995).

Biases in the sample are inevitable. Many of the stars have several time series, spanning different time scales. If these series span a time scale that is much shorter than the time scale of the intrinsic variations, then they will underestimate the variability since they are effectively just repeated observations of the star in the same state. In addition, one must keep in mind that while Si IV may be the dominant ion in B supergiant winds, it is only a trace ion in O star winds, so it may be capturing a completely different aspect of the wind in each case.

Table 1 presents some properties of the program stars. It lists the star name, the spectral type, the number of *IUE* spectra available, the number of days spanned by the data, the $v \sin i$ of the star from Howarth et al. (1997) and the maximum stellar rotation period, P_{max} . Stellar radii are needed to calculate P_{max} . The M_V were determined using V , $E(B - V)$, the distance (from either *GAIA* or *Hipparcos*) and the assumption that $R(V) = 3.1$. Then, using the T_{eff} s derived in § 3, and the bolometric corrections from Searle et al. (2008) for the B stars or Martins et al. (2005) for the O stars, we obtained the stellar radii. These are then combined with the observed $v \sin i$ to arrive at the P_{max} values given in the table.

For HD 47240, the *GAIA* data yielded an unrealistic result, implying an $M_V = -8.2$ mag, and $R/R_\odot = 66.0$. However, this is a normal B1 Ib whose $v \sin i$ of 100 km s^{-1} is somewhat high for a supergiant. Consequently, we assigned it an $M_V = -5$ mag, which is typical for its spectral type, and use that to calculate P_{max} .

All of the *IUE* data presented in this article were obtained from the Mikulski Archive for Space Telescopes (MAST) at the Space Telescope Science Institute. The specific observations analyzed can be accessed via DOI: 10.17909/d72e-de92.

3. MODELING THE WIND LINE VARIABILITY

In order to translate flux variations into the physical parameters needed to estimate the intrinsic error in a single \dot{M} measurement, a model is required. We use the SEI Sobolev model as formulated by Lamers et al. (1987) and modified by Massa et al. (2003). We note that the results described in the following sections imply that some of the assumptions inherent in the SEI model (such as spherical symmetry) are incorrect. However, this is unavoidable since these same results suggest that no current model is strictly correct. Another simplification of the SEI model is that it is a "core-halo" model, making it unreliable at low velocity. However, more sophisticated models, e.g., CMFGEN (Hillier 1990) or PoWR (Hamann & Koesterke 1998), require introducing additional, ill-defined parameters and assumptions, such as micro- and macro- clumping (Oskinova et al. 2006), the velocity law of the wind-photosphere interface and the assumption that the photosphere is homogeneous). Further, these models entail the computation of millions of lines in NLTE, making them ill-suited for the least squares process that we use, since it requires many tens or more re-computations for each fit. Consequently, it seems reasonable to concentrate on the nature of the wind beyond about 1.5 stellar radii using the simplest possible model in order to minimize the number of free parameters. This approach is simple and its output well-defined, making it a useful guide for the further development of the more sophisticated models. And importantly, the SEI model can be calculated quickly, making it ideal for use in an automated fitting procedure for a large number of spectra.

The calculation of an SEI profile requires the following parameters: a value for the terminal velocity, v_∞ ; a velocity law, typically a β law of the form $w = (1 - a/x)^\beta$, where $x = r/R_\star$, $w = v/v_\infty$, and

$a = 1 - w(x = 1)^{1/\beta}$; the turbulent velocity of the wind, w_D , and the radial (Sobolev) optical depth of the wind

$$\tau_{rad}(w) = Const \frac{\dot{M}}{R_* v_\infty^2} q_i(w) \left(x^2 w \frac{dw}{dx} \right)^{-1} \quad (1)$$

where $Const$ contains atomic parameters and q_i is the ionization fraction, which is assumed to be constant. The function $\tau_{rad}(w)$ is modeled by 20 velocity bins adjusted to obtain the best fitting profile. We also set $w(x = 1) = 0.01$ throughout. *Note that τ_{rad} variations are proportional to derived \dot{M} variations.*

In addition to the usual parameters, we also allow the ratio of the oscillator strengths of the doublets, f_B/f_R , to vary. This is a well known means to mimic the effect of optically thick structures partially covering the stellar disk (Prinja & Massa 2010). It also provides an additional diagnostic of how the portion of the wind structures in front of the star varies with time. We note that letting f_B/f_R be free has little impact on τ_{rad} . Its main effect is to improve the SEI fit to both components of the wind doublet. All of these parameters are determined by a non-linear least squares fit to the observed profile.

The fitting process involved the following three steps.

1. Preparation of the model photospheric spectrum: We used a simple visual comparison between the photospheric lines in the SWP spectrum and those of a grid of TLUSTY model atmospheres described by Hubeny et al. (2024)¹. The values of $v \sin i$ and the radial velocity, v_{rad} , are also adjusted in this process. We are not concerned with the accuracy of the atmospheric parameters (we simply require a match to the photospheric spectrum near the wind line), but the results are typically close to expectations. The normalization of the model atmosphere is performed using a version of the Fitzpatrick & Massa (1990) extinction parameters, and a model hydrogen atom to fit the interstellar Ly α absorption.

2. A grid search for v_∞ and β : Using the mean spectrum and a few individual spectra we perform a grid search to determine the v_∞ and β that produce the best fits. We also examine the blue edge of C IV $\lambda 1548$ (which is heavily saturated in the program stars) as a guide. This grid search involves a non-linear least squares fit using the routine developed by Markwardt (2009) to find the best τ_{rad} and w_D , with v_∞ and β fixed for each fit. For the β search, we placed additional weight on the emission portion of the profile, since it is formed by the entire wind and should be most indicative of the global properties of the wind. We fix the photospheric model, β and v_∞ for the star in subsequent fitting. These parameters are listed in Table 2 which gives the name of the star, its spectral type, and the T_{eff} , $\log g$ and turbulent velocity, v_t , of the model atmosphere used for the photospheric spectrum. It also gives the values adopted for the radial velocity and terminal wind velocity.

3. A least squares fit for $\tau_{rad}(w)$, w_D , and f_B/f_R : We then performed a non-linear least squares fit to each spectrum with the following independent variables: 20 independent bins to characterize $\tau_{rad}(w)$, w_D and f_B/f_R . In the fitting, we give the emission portion of the profile 30% of the weight allotted to the absorption because the emission originates throughout the wind, and is only weakly variable. In contrast, we are interested in the highly variable absorption, which is formed in a cylinder

¹ The new model atmospheres have 739,791 points which cover $200\text{\AA} \leq \lambda \leq 32\mu$ with an $R = 100,000$. They include models with $15 \leq T_{eff} \leq 55$ kK, $0.1 \leq Z/Z_\odot \leq 3.0$ and microturbulent velocities, v_t , of 2, 5 and 10 km s⁻¹.

between the observer and the stellar disk and is not expected to correspond to the global emission at any given time.

Repeating this process, we fit 1713 spectra of the 25 stars listed in Table 1. Each fit results in a τ_{rad} , f_B/f_R and w_D for that spectrum. Fourteen of the fits ($< 1\%$) were very poor for various reasons and rejected. This left 1699 fits for analysis. Figure 2 shows examples of the fits for a range of temperatures. When examining the fits, recall that the emission component is given a low weight since it originates throughout the wind.

4. ANALYSIS

In this section we first examine the time dependence of some properties of the fits for stars which have time series. Next, we examine the parameters that characterize the mean results of the fits for all of the stars, in order to search for any relationships that may emerge when the entire sample is considered. But first, we must define some notation.

4.1. Notation

We label a parameter, say x , derived from the i -th observation of the n -th star in sample as $x_i^{(n)}$. Each fit produces 22 parameters: 20 τ_{rad} bins, f_B/f_R , and w_D . With so many spectra to analyze, we distilled the τ_{rad} data into a single quantity. For each spectrum, we find the mean of $\tau_{rad}(w)$ over the normalized velocity range $w_1 \leq w \leq w_2$. We use $w_1 = 0.3$ and $w_2 = 1.0$. We adopt 0.3 for w_1 , because the optical depth at low w can be strongly influenced by the exact nature of the photospheric profile when the wind absorption is not very strong. Specifically, the averaging for the i -th spectrum of the n -th star is defined as

$$\tau_i^{(n)} = \langle \tau_{rad}(w_1 < w < w_2)_i^{(n)} \rangle \quad (2)$$

To simplify the notation, we define $r_i^{(n)}$ as the ratio of the blue and red f -values of the doublet determined by the fit, i.e.,

$$r_i^{(n)} \equiv f_{Bi}^{(n)} / f_{Ri}^{(n)} \quad (3)$$

Thus, each of the 1699 spectra are characterized by the following three parameters: $\tau_i^{(n)}$, $r_i^{(n)}$, and $w_{Di}^{(n)}$.

In addition, we summarize all of the parameters for the n -th star in terms of their mean and standard deviations with the following notation: $\tau^{(n)}$, $\sigma(\tau^{(n)})$, $r^{(n)}$, $\sigma(r^{(n)})$, and $w_D^{(n)}$, $\sigma(w_D^{(n)})$. We also examined the cross correlation coefficients of all of the variables, but only the one relating $\tau_i^{(n)}$ and $r_i^{(n)}$ proved to be of interest. It is denoted as $\rho(\tau_i^{(n)}, r_i^{(n)})^{(n)}$. Finally, we note that we often omit the superscript (n) when it is obvious that we are referring to a specific star.

4.2. Errors in the model parameters

The errors affecting the model parameters were estimated using a Monte Carlo procedure that is described in the Appendix. The results are listed in Table 5, where we see that the relative error ranges are: $0.02 \leq \sigma(r)/r \leq 0.08$, $0.02 \leq \sigma(w_D)/w_D \leq 0.14$, and $0.04 \leq \sigma(\tau)/\tau \leq 0.10$, with an RMS of 0.059. These results show that the estimates of our model parameters are quite robust.

4.3. Temporal variability of the parameters

Although our primary goal is to examine how wind line variability affects \dot{M} measurements, the large volume of data also presents an opportunity to examine how the different parameters might be

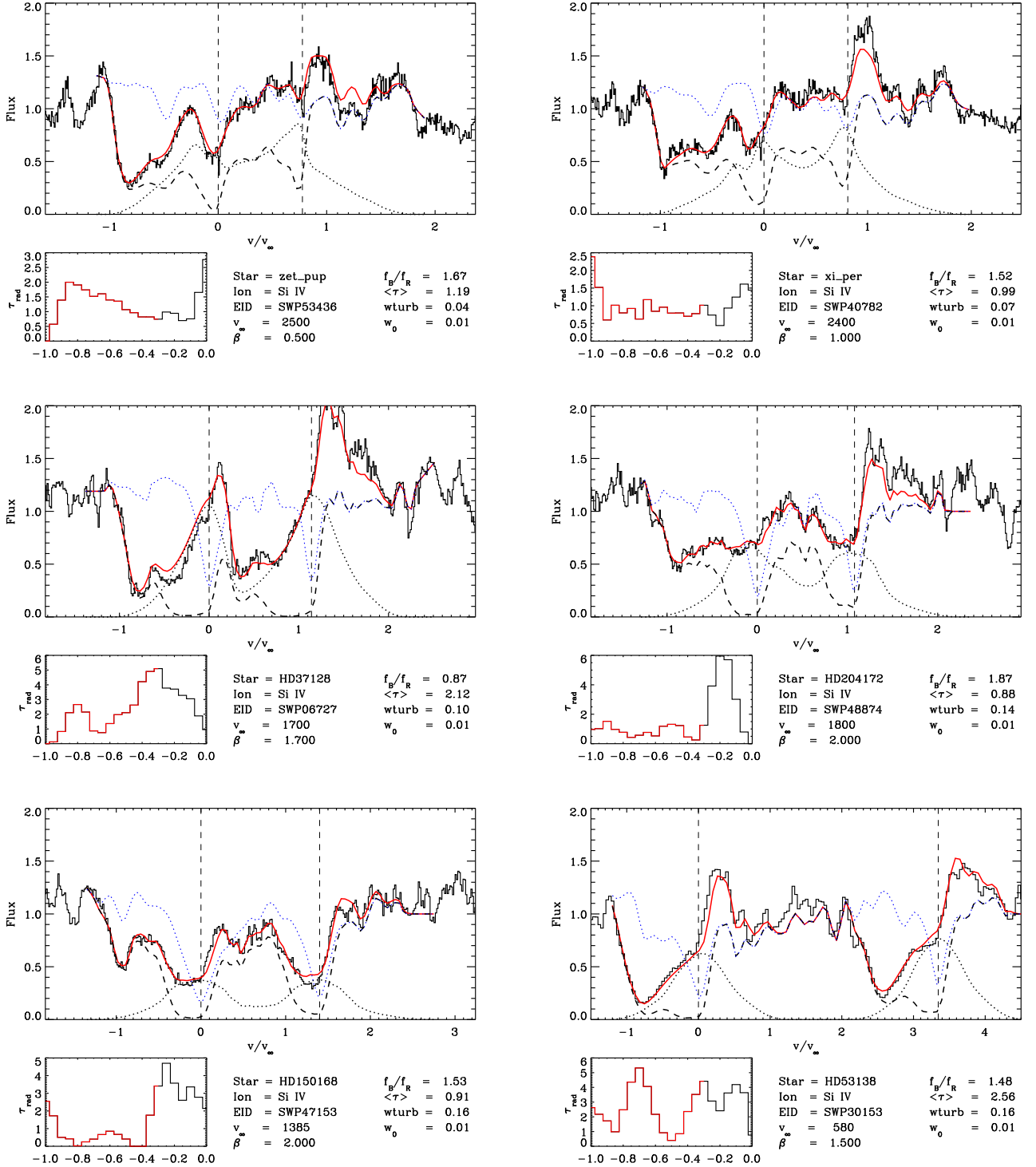


Figure 2. Examples of fits for a range of spectral types. Each panel lists the name of the star, the *IUE* spectrum fit and the fit parameters (where $w_{turb} \equiv w_D$). The figures show the observed spectrum (solid black), the photospheric spectrum used (bue dotted), the fit (solid red), the emission contribution (black dotted), the absorption component (dashed black) and the rest wavelengths of the doublet (vertical dashed). The insert is τ_{rad} versus v/v_∞ , where the red portion is that used to obtain the $\tau_i^{(n)}$ measurements.

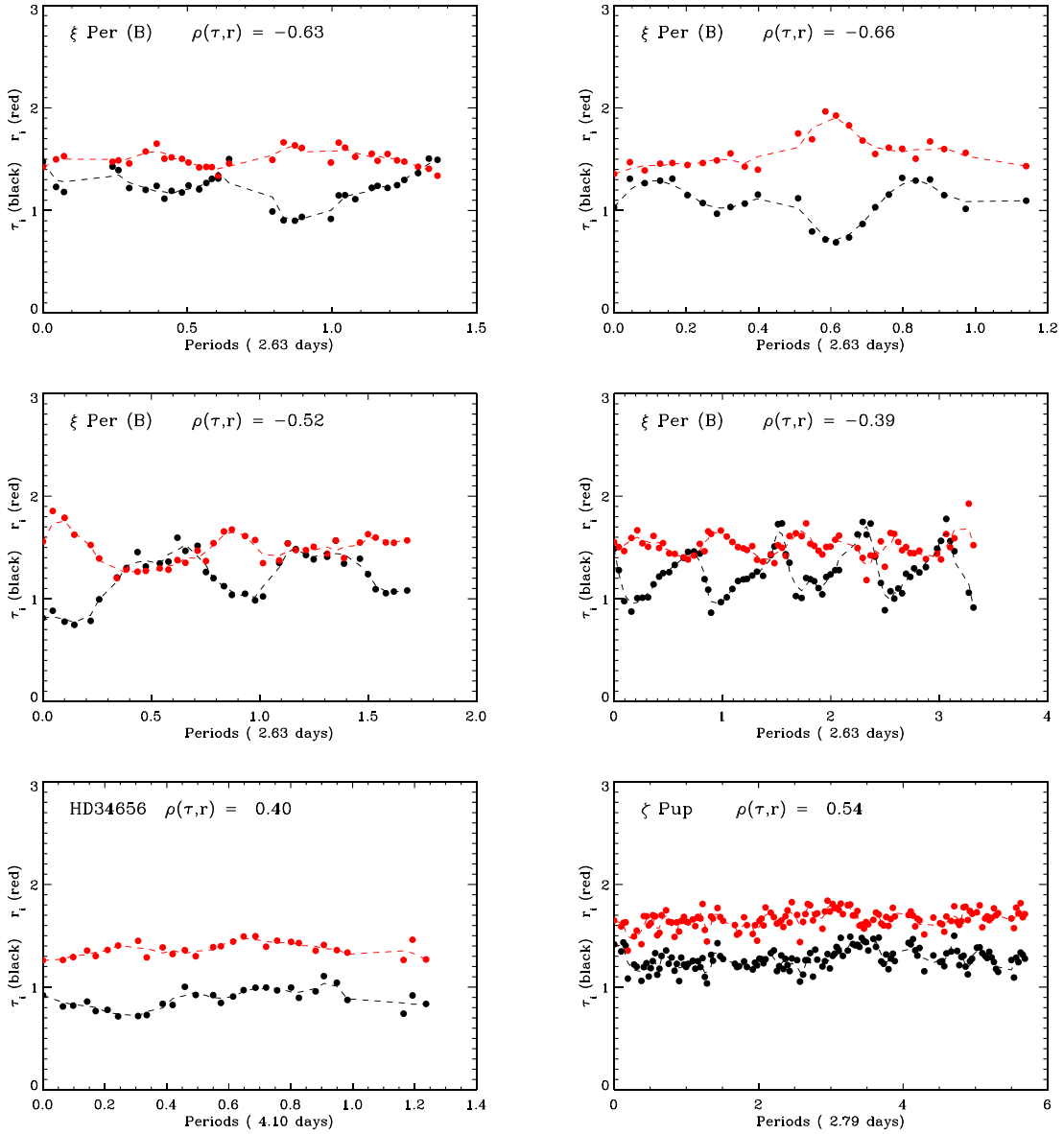


Figure 3. Plots of τ_i and r_i against time, in units of the maximum rotation period for stars with time series, as defined in the text. The dashed lines are three point smoothed versions of the points. The name of the star and correlation coefficient between τ and r are also shown in each panel. For stars with multiple series, the plots are ordered chronologically left-to-right, top-to-bottom. Stars with a (B) after their name have bowed structures in their dynamic spectra.

related and how they behave as functions of time. Because it is known that wind lines change on time scales related to the stellar rotation period (Prinja 1988), we concentrate on stars with 10 or more observations spanning at least one rotation period. Further, we only consider a set of observations as a series if it does not contain gaps larger than 20% of the period. Our search resulted in 19 series for 9 stars. These series are summarized in Table 3, which lists the star names, number of spectra

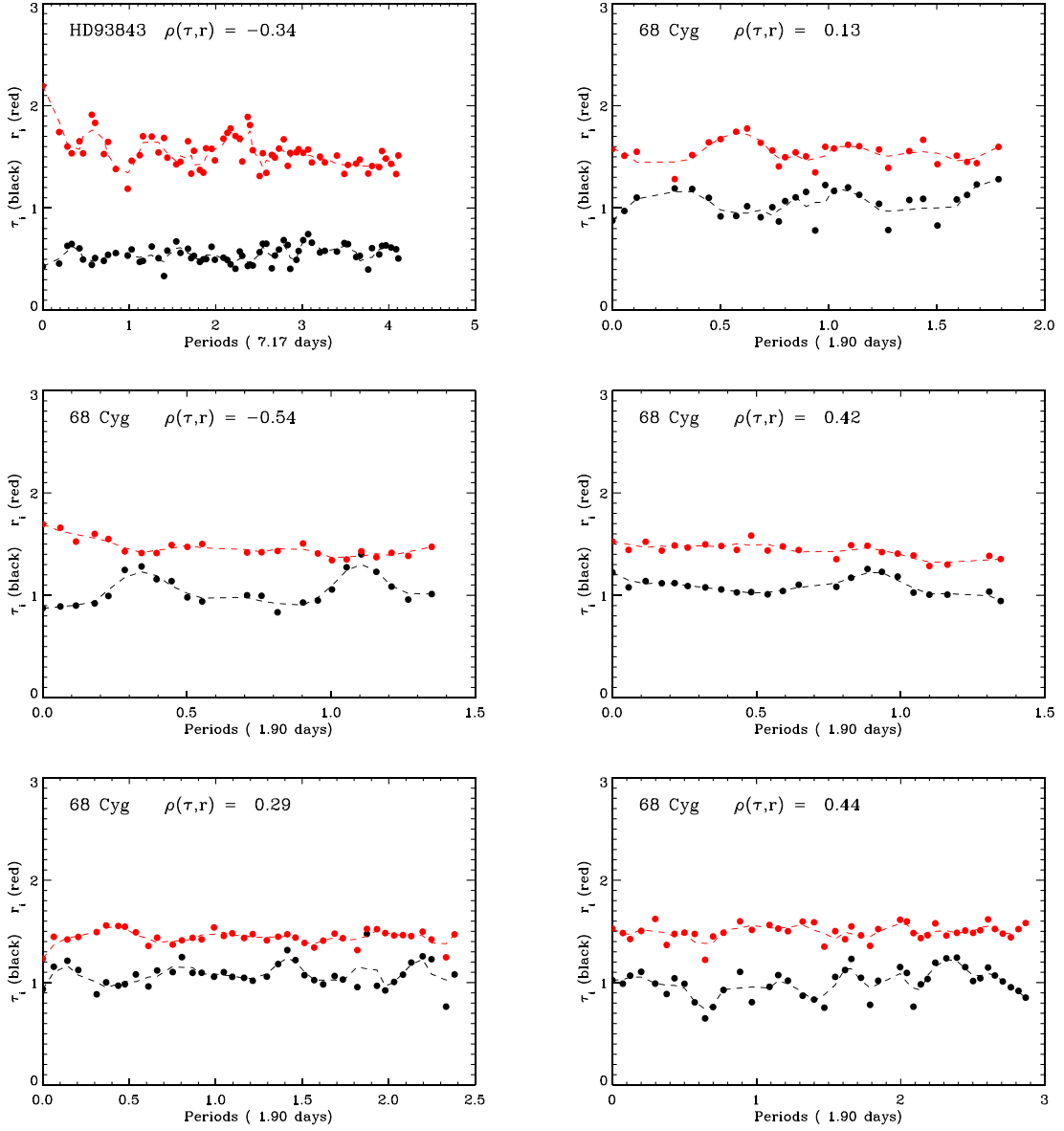


Figure 4. Same as Figure 3.

in the series, the time spanned by the series and the date of the *IUE* observations, and the τ , r and $\rho(\tau, r)$ for each series.

Figures 3 – 6 are plots of τ_i and r_i versus time (in periods) for the time series. Some stars have more than one series and most of these data sets are well known and have been described in detail before. Multiple plots for the same star are presented chronologically. Each plot gives the name of the star and $\rho(\tau, r)$ for the series. The following are descriptions of each series.

ξ Per: There are four series that qualify for this star. The longest one was described and analyzed in detail by de Jong et al. (2001). Its dynamic spectrum contains features termed bowed structures

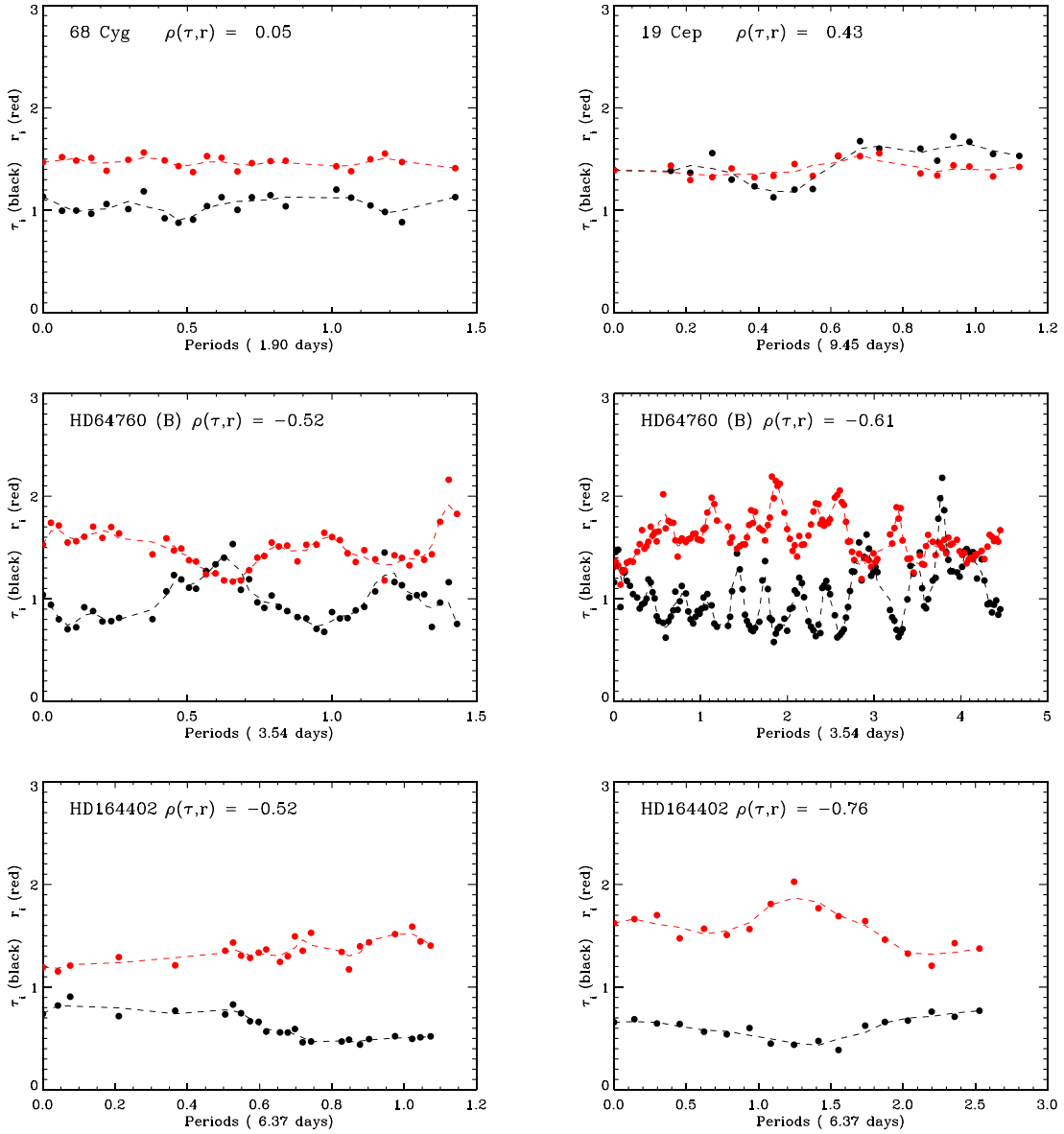


Figure 5. Same as Figure 3.

or bananas, which are indicative of spiral structures in the wind, viewed near $\sin i = 1$ (Cranmer & Owocki 1996). For this star, the variations in both τ_i and r_i are quite strong and anti-correlated. All of the series appear to contain at least one strong maximum per revolution period.

HD 34656: There is one series for this star, and it was examined previously by Kaper et al. (1996). For this star, the variations measured by τ_i and r_i are not very strong and are weakly, positively correlated with one another.

ζ Pup: This star was part of the *IUE* MEGA campaign (Massa et al. 1995), and analyzed in detail by Howarth et al. (1995). In spite of its dynamic spectrum showing significant variations, the

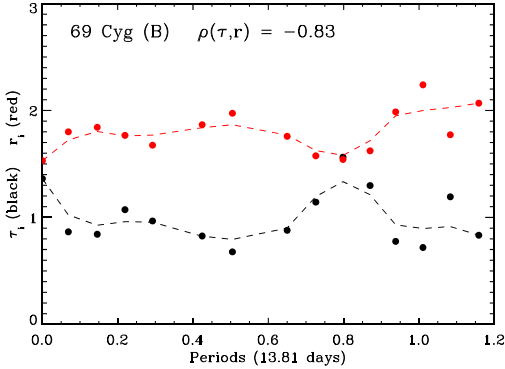


Figure 6. Same as Figure 3

variability measured by τ_i is quite weak and poorly correlated with r_i . This is because the variations seen in dynamic spectra of ζ Pup are not bowed. As a result, at any given time, there are positive and negative variations present in the profiles, and our broad band measure of optical depth can suppress such variations.

HD 93843: [Prinja et al. \(1998\)](#) presented a dynamic spectrum of the one series for this star and analyzed it in detail. Its dynamic spectrum shows no sign of bowed structures. The variations in τ_i are not very strong and are weakly anti-correlated with r_i .

68 Cyg: There are six series for this star, and the dynamic spectra have been described by [Kaper et al. \(1996\)](#) and [Massa & Prinja \(2015\)](#). The last two series are very close in time and are described as a single series by [Massa & Prinja \(2015\)](#). A particularly interesting aspect of these series is that τ and r are strongly anti-correlated at some epochs, and correlated at others. This change of behavior might be related to the fact that this star has the largest $v \sin i$ of all the stars listed in Table 1. In fact, recently [Britavskiy et al. \(2023\)](#) measured a $v \sin i$ of 323 km s^{-1} for this star. It is possible that the spiral structures have difficulty becoming organized or are easily disrupted by the rapid rotation.

19 Cep: [Kaper et al. \(1996\)](#) discussed the available data for this star. They presented five series, but only one has a time span covering more than an entire rotation period. None of the dynamic spectra indicate the presence of bowed structures. The τ_i variations are not very strong and are positively correlated with those in r_i .

HD 64760: There are two series for this star and [Fullerton et al. \(1997\)](#) analyzed them in detail. The dynamic spectra show the signatures of bananas, and were analyzed in terms of the co-rotating interaction region (CIR) model, but any process that creates a spiral pattern in the wind will do. As pointed out by [Fullerton et al. \(1997\)](#), features in the shorter, 1993 series, seem to repeat once per rotation while those in the 1995 series repeat twice per revolution. In both series, variations in τ_i and r_i are strong and highly anti-correlated.

HD 164402: This star has two series, previously described by [Prinja et al. \(2002\)](#). Both plots seem to contain a broad feature which spans more than a rotation period. However, one must remember that the maximum period uses the adopted value $v \sin i = 75 \text{ km s}^{-1}$. If this is too large by only about 20 km s^{-1} , then the variation would fit into a single period. In any case, variations in τ_i and

r_i are strongly anti-correlated, even though there is no strong signature of bowed structure in the available dynamic spectra.

69 Cyg: Prinja et al. (2002) presented the dynamic spectrum for this star. Although not flagged as having a bowed structure, the dynamic spectra do show the broad band variations that are typical of such features. Figure 6, shows a strong anti-correlation between τ_i and r_i .

We note that stars whose dynamic spectra show bow shaped structures, or "bananas" tend to have two distinctive features in the plots shown in Figs. 3 – 6. The first is that the variability is considerably larger than those without bananas. This is at least partly a natural consequence of the broad band definition of the $\tau_i^{(n)}$, since the bananas are also broad band features. The second is that r_i and τ_i are generally strongly anti-correlated for stars with bowed structure in their dynamic spectra. Even HD 150168, which was identified by Prinja et al. (2002) as having such structure, but is not included because its series only spans 0.85 periods, also has a large variance in τ_i which is anti-correlated with r_i .

We also examined the time dependence of the parameter w_{Di} , which also varies smoothly as a function of time. Usually it is not obviously related to either τ_i or r_i . The two exceptions are stars with strong bananas: ξ Per and HD 64760. In these cases, w_{Di} varies in phase with τ_i .

4.4. Global properties of the variability

In dealing with the entire sample of stars listed in Table 1, we examine the parameters, τ and $\sigma(\tau)$, r and $\sigma(r)$, and w_D and $\sigma(w_D)$ defined in section 4.1. These are just the means and standard deviations of the τ_i , r_i and w_{Di} determined from the fits to each spectrum for a particular star. We also examined the cross correlation coefficients between the different variables, and only $\rho(\tau, r)$ showed any systematic behavior. The results are listed in Table 4 which gives the star name, r , $\sigma(r)$, w_D , $\sigma(w_D)$, τ , $\sigma(\tau)$, $\sigma(\tau)/\tau$ and $\rho(\tau, r)$.

Because one of our main goals is to quantify relative errors in \dot{M} , the important parameter to consider is $\sigma(\tau)/\tau$, since it is proportional to $\sigma(\dot{M})/\dot{M}$. We examined all permutations of the variables described above, and selected results are shown in Figure 7. The only fit parameter that shows a significant correlation with $\sigma(\tau)/\tau$ is $\rho(\tau, r)$, and this is shown in the upper left of fig. 7. This reflects what was seen in the temporal plots. There, we noted that the stars whose dynamic spectra showed bowed structure also had large variations in τ_i , and that r_i and τ_i tended to be anti-correlated, $\rho(\tau, r) < 0$.

In addition to the wind line measurements, we also have the following ancillary data at our disposal: T_{eff} , $v \sin i$, v_∞ , and P_{max} . Some of these are also shown in Figure 7. The upper right plot shows that τ is independent of T_{eff} . This is expected since our sample was selected to have well developed but unsaturated Si IV wind lines. In contrast, the middle left plot shows that the fractional scatter increases with decreasing T_{eff} . The middle right plot shows that $\sigma(\tau)/\tau$ is also strongly correlated with v_∞ . However, this arises because v_∞ and T_{eff} are strongly correlated for our sample (see the lower left plot). This correlation may arise because our sample constrains the optical depth of the Si IV λ 1400 Å doublet to a narrow range, effectively confining the sample to a narrow slice across the HRD, with the cooler stars being more luminous.

Examination of the plots between the ancillary data and our derived parameters shows that there is no relation between r or $\sigma(r)$ and any of the ancillary data. The same is true for w_D , with the

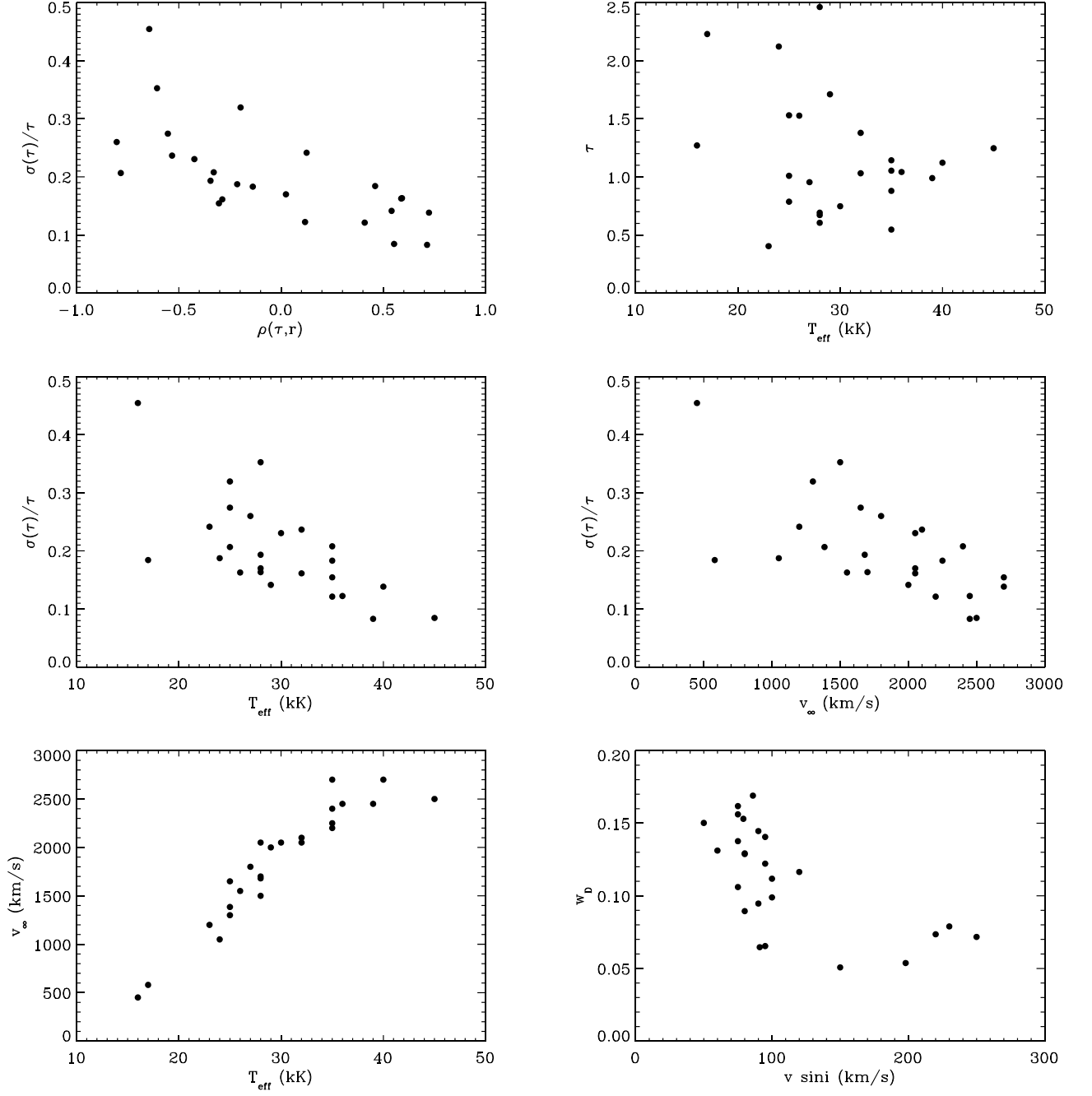


Figure 7. Plots of various parameters against each other. Top left, $\sigma(\tau)/\tau$ versus the correlation coefficient between τ and r . Top right, τ versus T_{eff} . Middle left, $\sigma(\tau)/\tau$ versus T_{eff} . Middle right, $\sigma(\tau)/\tau$ versus v_{∞} . Lower left, v_{∞} versus T_{eff} . Lower right, w_D versus $v \sin i$.

exception of w_D and $v \sin i$, shown in lower right plot of Figure 7. It suggests that w_D is smaller in stars with larger $v \sin i$ values.

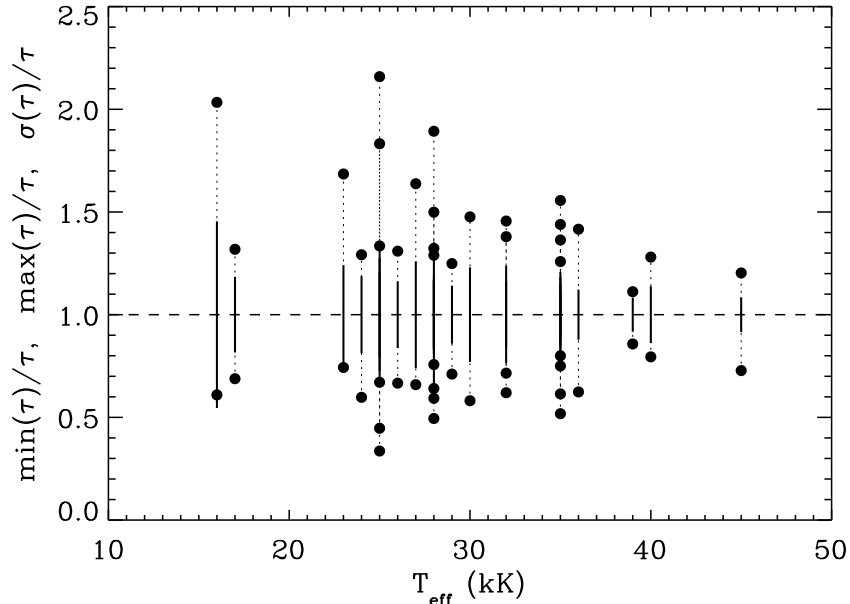


Figure 8. The maximum and minimum values of τ_i for each star divided by the mean value, τ , and $\sigma(\tau)/\tau$. There is one set of points for each star. The vertical dotted lines connect the maximum and minimum values of τ_i/τ and the thick bars are $\pm 1\sigma(\tau)/\tau$.

5. DISCUSSION

The discussion addresses two separate issues. The first involves the implications of our results on any measurement of \dot{M} , and is purely empirical. The second concerns how the relationships we have uncovered can be interpreted in physical terms.

Throughout the discussion, we must keep in mind that our sample is biased. The stars were selected to have Si IV wind lines that are well developed, but unsaturated. For the later type stars, Si IV may be the dominant Si ion in the wind. However, for the earlier stars, it may only be a trace ionization stage, with most of the Si in Si V. Consequently, the Si IV 1400 doublet may be sampling very different components of the wind in the coolest and hottest stars in our sample.

5.1. Empirical implications

In this section, we assess and quantify the intrinsic accuracy of \dot{M} measurements. Since τ_{rad} is directly proportional to \dot{M} , variations in τ_{rad} are surrogates for variations in \dot{M} measurements. Regardless of whether the optical depth variations are due to changes in the ionization fraction, q , or the velocity gradient, dw/dx , the result is the same: the *measured* \dot{M} will change proportionally. Thus, for the purpose of determining the intrinsic error, it does not matter what causes the variations in the τ_i .

For each star, Figure 8 shows the maximum and minimum measured values of τ_i divided by the mean and $\sigma(\tau)/\tau$ plotted against T_{eff} . These are representative of the error expected from a single observation. The results imply an RMS intrinsic error between 8% and 45%, with an average of 22%.

Further, the figure shows that a single determination can have an error as large as a factor of two or more. There is also an indication that the errors are larger for cooler stars and smaller for hotter stars.

For nearly all of the stars, the errors derived in section 4.2 are much smaller than the observed variations. There are, however, two exceptions: ζ Pup and HD 190429. As discussed in section 4.3, our broad band measure of optical depths suppressed the profile variations that are known to be present in ζ Pup. However, HD 190429 has not been closely studied for variability. Although there are 16 *IUE* observations of it, these effectively sample only 4 independent epochs. There is one observation in 1979, thirteen in 1990 (all obtained within 2 days), one in May of 1995 and the last in September of 1995. Close examination of the 4 independent epochs shows no detectable variations in the Si IV profile. Thus, it appears that the wind lines of HD 190429 do not vary at a level detectable by *IUE*. That makes HD 190429 the only star in our sample whose wind lines may not vary.

Overall, the current discussion suggests that one should not place too much weight on a single observational determination of \dot{M} , and that two or more observations, well separated in time, are much more reliable.

5.2. Physical implications

In this section, we examine our results for clues that may provide a deeper understanding of the physical processes responsible for the variability. It is important to understand the geometry of the structures causing the optical depth variations, since radiation transfer through optically thick structures depends on the geometry.

We interpret our results in terms of the simple model proposed by Cranmer & Owocki (1996), which predicts that spiral structures in the wind are responsible for the variability. In addition, we also assume that the spiral structures are optically very thick, in accordance with the results of Prinja & Massa (2010).

In this model, the bowed structures in the dynamic spectra of stars viewed with $\sin i \simeq 1$ result from the way a spiral arm exits the line of sight to the stellar disk. The portion that exits first absorbs at over a large range of intermediate velocities, so the absorption lessens there first. This effect is illustrated by Figure 12 in Fullerton et al. (1997). However, when $\sin i$ is much less than 1, the portion of the arm that exits the line of sight first absorbs near $v = 0$, and the effect is lost. Thus, we assume that although spiral structures are responsible for most, or possibly all, of the variability, stars whose dynamic spectra contain bowed structures have $\sin i \simeq 1$.

With this model in mind, we note that Figs. 3 – 6 shows that for stars with bowed structures in their dynamic spectra when τ_i increases, r_i decreases. This indicates that when the overall measured opacity is larger, so is the covering factor, reflected in the decrease in r_i . Such an effect is consistent with the model, where the measured absorption is strongly influenced by how much of the line of sight to the stellar disk is obscured by the optically very thick structures in the wind. In two cases (ξ Per and HD 64760) when τ_i is large, w_{Di} is too. This suggests that a more turbulent flow is present when the wind along the line of sight is composed of two very distinct flows.

A second interesting result is that $\sigma(\tau)/\tau$ appears to decrease with increasing T_{eff} . We cannot be certain whether this is simply because none of the earliest stars happen to have $\sin i \simeq 1$ or that the wind structure is intrinsically different. However the fact that ζ Pup has a large $v \sin i$ (suggesting its $\sin i \simeq 1$) but does not have strongly bowed structures, bolsters the notion that the winds of the earliest stars are, in fact, different. It is quite possible that the spirals that give rise to the bowed

structures are disrupted by the more powerful winds in the earliest stars and fragment into a more random distribution of clumps.

6. SUMMARY

We reviewed the evidence that wind line variability is universal and probably due to large, spatially coherent spiral structures. These structures extend to the base of the wind and cover much of the stellar disk. Further, they are denser than their surroundings and, because they are optically thick, *their geometry matters*.

We then modeled the Si IV wind doublet in 1699 spectra of 25 stars. This allowed us to determine $\sigma(\tau)/\tau$, which is directly proportional to any $\sigma(\dot{M})/\dot{M}$ estimate derived from fitting the Si IV doublet. For the entire sample, we found that $\sigma(\tau)/\tau \simeq 0.22$, implying an intrinsic error of $\simeq 22\%$ in any \dot{M} measurement. We also showed that it is quite possible that a single observation can differ from the mean by as much as a factor of two. In addition, there is an indication that the magnitude of the errors depends on the stellar temperature, being larger for the B and late O stars and smaller for the hottest O stars.

In analyzing the available time series, we discovered that, for many stars, variations in both the optical depths and the ratios of the f values are cyclical and 180° out of phase. This is particularly strong for stars whose dynamic spectra contain bowed structures. We argue that these stars likely have $\sin i \simeq 1$, and that the relationship is an indication that the increase in measured optical depth is the result of optically very thick structures occulting more of the line of sight to the stellar disk. We also noted that, for our sample, the variations in τ are smaller for the hottest stars and they are not anti-correlated with the ratio of f values. This raises the possibility that the spiral structures are torn apart in the stars with the most powerful winds.

D.M. acknowledges support from NASA ADAP grant 80NSSC22K0492 and NASA HST grants HST-GO-16230.001-A and HST-GO-16182.002. L.O. acknowledges support from Deutsche Forschungsgemeinschaft (DFG) grant GZ: OS 292/6-1. We also thank the referee for useful comments that helped clarify the presentation.

Facilities: Simbad, IUE, MAST, GAIA

APPENDIX

A. ERRORS IN THE MODEL PARAMETERS

In this appendix, we explain how we estimated the errors affecting the parameters derived from the non-linear least squares fits. We began by randomly selecting one spectrum for each program star, $f(\lambda)_0$. Together with the errors for this spectrum, $\sigma(\lambda)$ (described below), we generated a wavelength array of normally distributed random numbers with standard deviations of $\sigma(\lambda)$. This array, $\epsilon(\lambda)$, was then added to the original spectrum, $f(\lambda)^{(n)} = f(\lambda)_0 + \epsilon(\lambda)^{(n)}$. The process was then repeated 100 times to create copies of the original spectrum including the effects of errors. Each of these 100 spectra were then fit by our model, using the same photospheric spectrum, v_∞ , and β . Finally, the scatter in the derived model parameters were used to estimate their errors.

As mentioned above, the analysis requires the expected error at each wavelength, $\sigma(\lambda)$. Unfortunately, the error arrays accompanying the NEWSIPS spectra are not appropriate for our analysis. This is because they include an off-set error due to thermal changes in the focus of the *IUE* telescope and imprecise centering of the star in the *IUE* aperture. These errors are especially large for small aperture spectra, since the stellar image overfilled the small aperture. In contrast, our data are not affected by this error because all of the spectra are normalized over a spectral band near Si IV. Consequently, we had to determine the errors that are appropriate for our spectra. This was done using the four program stars with 200 or more observations: ξ Per, ζ Pup, 68 Cyg, and HD 64760. For these stars, we simply calculated the standard deviation of the normalized spectra at each wavelength. We found that for wavelengths away from the intrinsically variable resonance lines, the $\sigma(\lambda)$ are proportional to the mean flux, regardless of whether the spectra were obtained through the large or small aperture. As a result, we adopted the relation, $\sigma(\lambda) = af(\lambda)_0$ to determine the errors, with $a = 0.06$. The results are presented in Table 5 which lists: the star name, the SWP number of the spectrum used in the analysis, the mean and standard deviation divided by the mean of the 100 trials for each of the model parameters: τ , r and w_D .

REFERENCES

- Britavskiy, N., Simón-Díaz, S., Holgado, G., et al. 2023, *A&A*, 672, A22.
- Cranmer, S.R. & Owocki, S.P. 1996, *ApJ*, 462, 469.
- de Jong, J. A., Henrichs, H. F., Kaper, L., et al. 2001, *A&A*, 368, 601.
- Ebbets, D. 1982, *ApJS*, 48, 399.
- Fitzpatrick, E. L. & Massa, D. 1990, *ApJS*, 72, 163.
- Fullerton, A. W., Massa, D. L., Prinja, R. K., et al. 1997, *A&A*, 327, 699.
- Fullerton, A.W., Massa, D.L., & Prinja, R.K. 2006, *ApJ*, 637, 1025.
- Hamann, W.-R. & Koesterke, L. 1998, *A&A*, 335, 1003
- Hillier, D. J. 1990, *A&A*, 231, 116
- Howarth, I. D., Prinja, R. K., & Massa, D. 1995, *ApJL*, 452, L65.
- Howarth, I. D., Siebert, K. W., Hussain, G. A. J., et al. 1997, *MNRAS*, 284, 265.
- Hubeny, I., Gordon, K. & Fitzpatrick, E.L. 2024, In preparation
- Kobulnicky, H. A., Chick, W. T., & Povich, M. S. 2019, *AJ*, 158, 73.
- Kaper, L., Henrichs, H. F., Nichols, J. S., et al. 1996, *A&AS*, 116, 257.
- Lamers, H.J.G.L.M., Cerruti-Sola, M., & Perinotto, M. 1987, *ApJ*, 314, 726.
- Lehner, N., Fullerton, A. W., Massa, D., et al. 2003, *ApJ*, 589, 526.
- Markwardt, C. B. 2009, *Astronomical Data Analysis Software and Systems XVIII*, 411, 251.
- Martins, F., Schaerer, D., & Hillier, D. J. 2005, *A&A*, 436, 1049.
- Massa, D., Fullerton, A.W., Nichols, J.S., et al. 1995, *ApJL*, 452, L53.
- Massa, D., Fullerton, A.W., Hutchings, J.B., et al. 2000, *ApJL*, 538, L47.
- Massa, D. & Prinja, R.K. 2015, *ApJ*, 809, 12.
- Massa, D., Fullerton, A. W., & Prinja, R. K. 2017, *MNRAS*, 470, 3765.
- Massa, D., Oskinova, L., Prinja, R. & Ignace, R. 2019, *ApJ*, 873, 81.
- Massa, D., Fullerton, A.W., Sonneborn, G., et al. 2003, *ApJ*, 586, 996.
- Nazé, Y., Oskinova, L.M., & Gosset, E. 2013, *ApJ*, 763, 143.
- Nazé, Y., Ramiaramanantsoa, T., Stevens, I.R., et al. 2018, *A&A*, 609, A81.
- Olson, G. L. 1982, *ApJ*, 255, 267.
- Oskinova, L.M., Clarke, D., & Pollock, A.M.T. 2001, *A&A*, 378, L21.
- Oskinova, L. M., Feldmeier, A., & Hamann, W.-R. 2006, *MNRAS*, 372, 313.
- Prinja, R. K. 1988, *MNRAS*, 231, 21P.
- Prinja, R. K. & Howarth, I. D. 1988, *MNRAS*, 233, 123.

- Prinja, R.K. & Howarth, I.D. 1986, ApJS, 61, 357.
- Prinja, R. K., Massa, D., Howarth, I. D., et al. 1998, MNRAS, 301, 926.
- Prinja, R.K., Massa, D.L., Urbaneja, M.A., et al. 2012, MNRAS, 422, 3142.
- Prinja, R.K., Massa, D., & Fullerton, A.W. 2002, A&A, 388, 587.
- Prinja, R.K. & Massa, D.L. 2010, A&A, 521, L55.
- Searle, S. C., Prinja, R. K., Massa, D., et al. 2008, A&A, 481, 777.
- Walborn, N. R., Nichols-Bohlin, J., & Panek, R. J. 1985, NASA Reference Publication, 1155.
- Walborn, N. R., Parker, J. W., & Nichols, J. S. 1995, NASA Reference Publication, 1363, 0.

Facilities: HST(MAST), IUE

Table 1. Program Stars

| Name | Sp Ty | N | Δt (days) | $v \sin i$ | P_{max} (days) |
|----------------|------------------|-----|-------------------|------------|------------------|
| ξ Per | O7.5 III(n)((f)) | 323 | 6036 | 230 | 2.63 |
| HD 34656 | O7 II(f) | 30 | 3364 | 91 | 4.10 |
| HD 36486 | O9.5 II | 58 | 4793 | 120 | 3.58 |
| ζ Pup | O4 I(n)f | 212 | 6271 | 198 | 2.79 |
| HD 93403 | O5 III(fc) var | 10 | 6050 | 100 | 12.06 |
| HD 93843 | O5 III(fc) | 69 | 5977 | 95 | 7.17 |
| μ Nor | O9.7 Iab | 34 | 3974 | 80 | 10.93 |
| HD 162978 | O7.5 II((f)) | 22 | 5700 | 86 | 5.89 |
| HD 190429 | O4 If+ | 16 | 6009 | 90 | 9.86 |
| 68 Cyg | O7.5 III:n((f)) | 227 | 6025 | 250 | 1.90 |
| HD 207198 | O9 Ib-II | 13 | 1827 | 80 | 8.07 |
| 19 Cep | O9.5 Ib | 133 | 6024 | 95 | 9.45 |
| ζ Per | B1 Ib | 14 | 370 | 75 | 13.07 |
| ϵ Ori | B0 Ia | 53 | 3080 | 75 | 22.08 |
| κ Ori | B0.5 Ia | 39 | 3079 | 95 | 7.03 |
| HD 47240 | B1 Ib | 21 | 5452 | 100 | 32.42 |
| σ^2 CMa | B3 Ia | 22 | 3001 | 50 | 85.51 |
| η CMa | B5 Ia | 11 | 3030 | 60 | 44.65 |
| HD 64760 | B0.5 Ib | 208 | 6073 | 220 | 3.54 |
| ρ Leo | B1 Iab | 12 | 6077 | 80 | 11.59 |
| HD 150168 | B1 Ia | 56 | 4944 | 120 | 6.13 |
| HD 164402 | B0 Ib | 62 | 5831 | 75 | 6.37 |
| HD 167756 | B0.5 Ia | 19 | 2811 | 79 | 8.66 |
| 69 Cyg | B0 Ib | 37 | 5151 | 75 | 13.81 |
| HD 219188 | B0.5 II-III(n) | 12 | 6024 | 150 | 3.28 |

Table 2. Stellar properties

| Name | Sp Ty | T_{eff} | $\log g$ | v_t | v_{rad} | v_{∞} |
|----------------|-----------------|------------------|----------|-------|------------------|--------------|
| ξ Per | O7.5III(n)((f)) | 35000 | 3.5 | 10.0 | 65 | 2400 |
| HD 34656 | O7 II(f) | 35000 | 3.5 | 10.0 | -12 | 2200 |
| HD 36486 | O9.5 IINwk | 30000 | 3.5 | 2.0 | 18 | 2050 |
| ζ Pup | O4 I(n)fp | 45000 | 3.0 | 10.0 | -24 | 2500 |
| HD 93403 | O5.5 III(fc)var | 40000 | 3.5 | 10.0 | -15 | 2700 |
| HD 93843 | O5 III(fc) | 35000 | 3.5 | 10.0 | -10 | 2700 |
| μ Nor | O9.7 Iab | 29000 | 3.5 | 10.0 | 6 | 2200 |
| HD 162978 | O7.5 II((f)) | 35000 | 3.5 | 10.0 | -12 | 2250 |
| HD 190429 | O4 If+ | 39000 | 3.5 | 10.0 | -16 | 2450 |
| 68 Cyg | O7.5 III:n((f)) | 36000 | 3.5 | 10.0 | 1 | 2450 |
| HD 207198 | O9 Ib-II | 32000 | 3.5 | 10.0 | -18 | 2100 |
| 19 Cep | O9.5 Ib | 32000 | 3.5 | 10.0 | -12 | 2050 |
| ζ Per | B1 Ib | 23000 | 3.5 | 10.0 | 21 | 1200 |
| ϵ Ori | B0 Ia | 28000 | 3.0 | 10.0 | 27 | 1700 |
| κ Ori | B0.5 Ia | 26000 | 3.5 | 10.0 | 20 | 1550 |
| HD 47240 | B1 Ib | 24000 | 3.0 | 10.0 | 33 | 1050 |
| σ^2 CMa | B3 Iab | 17000 | 3.0 | 10.0 | 48 | 580 |
| η CMa | B5 Ia | 16000 | 2.5 | 10.0 | 41 | 450 |
| HD 64760 | B0.5 Ib | 25000 | 2.5 | 10.0 | 41 | 1650 |
| ρ Leo | B1 Ib | 25000 | 3.5 | 10.0 | 42 | 1300 |
| HD 150168 | B1 Ia | 25000 | 3.0 | 10.0 | 6 | 1385 |
| HD 164402 | B0 Iab/b | 28000 | 3.0 | 10.0 | 4 | 1680 |
| HD 167756 | B0.5 Ib | 28000 | 3.5 | 10.0 | -25 | 2050 |
| 69 Cyg | B0 Ib | 27000 | 3.0 | 10.0 | 2 | 1800 |
| HD 219188 | B0.5 III | 28000 | 3.5 | 2.0 | 71 | 1500 |

Table 3. Series properties

| Name | N | Δt (days) | Date | τ | $\sigma(\tau)$ | $\sigma(\tau)/\tau$ | $\rho(\tau, r)$ |
|-------------|-----|-------------------|--------|--------|----------------|---------------------|-----------------|
| ξ Per | 33 | 3.59 | 9/87 | 1.22 | 0.17 | 0.14 | -0.63 |
| ξ Per | 25 | 3.00 | 10/88 | 1.08 | 0.19 | 0.18 | -0.66 |
| ξ Per | 36 | 4.42 | 10/91 | 1.21 | 0.24 | 0.20 | -0.52 |
| ξ Per | 68 | 8.72 | 10/94 | 1.26 | 0.23 | 0.18 | -0.39 |
| HD 34656 | 29 | 5.07 | 2/91 | 0.89 | 0.10 | 0.12 | 0.40 |
| ζ Pup | 139 | 15.86 | 1/95 | 1.28 | 0.10 | 0.08 | 0.54 |
| HD 93843 | 67 | 29.48 | 5/96 | 0.55 | 0.08 | 0.16 | -0.34 |
| 68 Cyg | 29 | 3.39 | 9/87 | 1.05 | 0.14 | 0.13 | 0.13 |
| 68 Cyg | 23 | 2.56 | 10/88 | 1.05 | 0.15 | 0.15 | -0.54 |
| 68 Cyg | 23 | 2.56 | 10/89 | 1.09 | 0.08 | 0.07 | 0.42 |
| 68 Cyg | 40 | 4.52 | 10/91 | 1.08 | 0.13 | 0.12 | 0.29 |
| 68 Cyg | 43 | 5.45 | 10/94a | 0.99 | 0.14 | 0.14 | 0.44 |
| 68 Cyg | 22 | 2.71 | 10/94b | 1.04 | 0.10 | 0.09 | 0.05 |
| 19 Cep | 18 | 10.60 | 10/94 | 1.45 | 0.18 | 0.12 | 0.43 |
| HD 64760 | 47 | 5.07 | 3/93 | 0.98 | 0.21 | 0.21 | -0.52 |
| HD 64760 | 148 | 15.77 | 1/95 | 1.04 | 0.29 | 0.28 | -0.61 |
| HD 164402 | 24 | 6.83 | 8/86 | 0.61 | 0.14 | 0.22 | -0.52 |
| HD 164402 | 17 | 16.10 | 3/95 | 0.61 | 0.11 | 0.19 | -0.76 |
| 69 Cyg | 15 | 16.00 | 10/93 | 1.00 | 0.26 | 0.26 | -0.83 |

Table 4. Derived parameters

| Name | r | $\sigma(r)$ | w_D | $\sigma(w_D)$ | τ | $\sigma(\tau)$ | $\sigma(\tau)/\tau$ | $\rho(\tau, r)$ |
|----------------|------|-------------|-------|---------------|--------|----------------|---------------------|-----------------|
| ξ Per | 1.49 | 0.15 | 0.08 | 0.02 | 1.14 | 0.24 | 0.21 | -0.33 |
| HD 34656 | 1.37 | 0.07 | 0.06 | 0.02 | 0.88 | 0.11 | 0.12 | 0.41 |
| HD 36486 | 1.18 | 0.15 | 0.12 | 0.03 | 0.75 | 0.17 | 0.23 | -0.42 |
| ζ Pup | 1.63 | 0.13 | 0.05 | 0.01 | 1.25 | 0.11 | 0.08 | 0.55 |
| HD 93403 | 1.23 | 0.21 | 0.10 | 0.01 | 1.12 | 0.16 | 0.14 | 0.72 |
| HD 93843 | 1.54 | 0.17 | 0.07 | 0.01 | 0.55 | 0.08 | 0.15 | -0.30 |
| μ Nor | 1.19 | 0.13 | 0.13 | 0.02 | 1.71 | 0.24 | 0.14 | 0.54 |
| HD 162978 | 1.31 | 0.09 | 0.17 | 0.02 | 1.05 | 0.19 | 0.18 | -0.14 |
| HD 190429 | 1.12 | 0.08 | 0.09 | 0.01 | 0.99 | 0.08 | 0.08 | 0.71 |
| 68 Cyg | 1.46 | 0.09 | 0.07 | 0.02 | 1.04 | 0.13 | 0.12 | 0.12 |
| HD 207198 | 1.49 | 0.20 | 0.09 | 0.01 | 1.03 | 0.24 | 0.24 | -0.53 |
| 19 Cep | 1.32 | 0.09 | 0.14 | 0.02 | 1.38 | 0.22 | 0.16 | -0.29 |
| ζ Per | 1.50 | 0.14 | 0.11 | 0.01 | 0.40 | 0.10 | 0.24 | 0.12 |
| ϵ Ori | 1.18 | 0.16 | 0.16 | 0.02 | 2.46 | 0.40 | 0.16 | 0.59 |
| κ Ori | 1.31 | 0.13 | 0.12 | 0.01 | 1.53 | 0.25 | 0.16 | 0.59 |
| HD 47240 | 1.21 | 0.19 | 0.11 | 0.02 | 2.12 | 0.40 | 0.19 | -0.21 |
| σ^2 CMa | 1.32 | 0.11 | 0.15 | 0.04 | 2.23 | 0.41 | 0.18 | 0.46 |
| η CMa | 1.64 | 0.28 | 0.13 | 0.03 | 1.27 | 0.58 | 0.45 | -0.64 |
| HD 64760 | 1.58 | 0.20 | 0.07 | 0.02 | 1.01 | 0.28 | 0.27 | -0.55 |
| ρ Leo | 1.46 | 0.11 | 0.13 | 0.01 | 1.53 | 0.49 | 0.32 | -0.20 |
| HD 150168 | 1.52 | 0.25 | 0.14 | 0.02 | 0.79 | 0.16 | 0.21 | -0.78 |
| HD 164402 | 1.42 | 0.18 | 0.16 | 0.01 | 0.60 | 0.12 | 0.19 | -0.34 |
| HD 167756 | 1.34 | 0.15 | 0.15 | 0.01 | 0.67 | 0.11 | 0.17 | 0.02 |
| 69 Cyg | 1.79 | 0.23 | 0.14 | 0.01 | 0.95 | 0.25 | 0.26 | -0.80 |
| HD 219188 | 1.29 | 0.23 | 0.05 | 0.02 | 0.69 | 0.24 | 0.35 | -0.61 |

Table 5. Parameter Errors

| Star | SWP | τ | $\sigma(\tau)/\tau$ | r | $\sigma(r)/r$ | w_D | $\sigma(w_D)/w_D$ |
|--------------|-------|--------|---------------------|-------|---------------|-------|-------------------|
| ξ Per | 52617 | 1.256 | 0.062 | 1.458 | 0.050 | 0.056 | 0.117 |
| HD 34656 | 40788 | 0.961 | 0.046 | 1.449 | 0.031 | 0.053 | 0.098 |
| HD 36486 | 28001 | 1.087 | 0.042 | 1.065 | 0.023 | 0.141 | 0.085 |
| ζ Pup | 36143 | 1.121 | 0.057 | 1.587 | 0.051 | 0.043 | 0.160 |
| HD 93403 | 47534 | 1.138 | 0.060 | 1.436 | 0.039 | 0.105 | 0.101 |
| HD 93843 | 57062 | 0.620 | 0.044 | 1.675 | 0.055 | 0.099 | 0.082 |
| HD 149038 | 27939 | 2.251 | 0.071 | 1.266 | 0.050 | 0.130 | 0.031 |
| HD 162978 | 30502 | 1.140 | 0.057 | 1.339 | 0.039 | 0.172 | 0.047 |
| HD 190429 | 38970 | 0.971 | 0.065 | 1.051 | 0.051 | 0.059 | 0.094 |
| 68 Cyg | 42821 | 1.118 | 0.051 | 1.434 | 0.039 | 0.100 | 0.051 |
| HD 207198 | 26001 | 1.432 | 0.070 | 1.321 | 0.042 | 0.081 | 0.130 |
| 19 cep | 31769 | 1.371 | 0.043 | 1.365 | 0.030 | 0.144 | 0.051 |
| HD 24398 | 03053 | 0.389 | 0.041 | 1.601 | 0.068 | 0.057 | 0.230 |
| HD 37128 | 24879 | 2.082 | 0.065 | 1.243 | 0.037 | 0.126 | 0.068 |
| κ Ori | 06733 | 1.273 | 0.046 | 1.250 | 0.028 | 0.106 | 0.046 |
| HD 47240 | 48873 | 2.214 | 0.065 | 1.530 | 0.040 | 0.089 | 0.040 |
| o^2 CMa | 30153 | 2.434 | 0.076 | 1.328 | 0.064 | 0.174 | 0.075 |
| η CMa | 30198 | 2.544 | 0.094 | 1.287 | 0.076 | 0.159 | 0.083 |
| HD 64760 | 53742 | 1.443 | 0.049 | 1.378 | 0.032 | 0.083 | 0.031 |
| HD 91316 | 11312 | 1.751 | 0.052 | 1.565 | 0.029 | 0.137 | 0.033 |
| HD 150168 | 47222 | 0.842 | 0.057 | 1.511 | 0.048 | 0.151 | 0.032 |
| HD 164402 | 54132 | 0.647 | 0.047 | 1.495 | 0.069 | 0.156 | 0.082 |
| HD 167756 | 29025 | 0.687 | 0.055 | 1.364 | 0.058 | 0.152 | 0.020 |
| HD 204172 | 38979 | 0.820 | 0.043 | 1.922 | 0.040 | 0.131 | 0.059 |
| HD 219188 | 53057 | 1.219 | 0.073 | 1.259 | 0.026 | 0.069 | 0.071 |